

Viscous detonation in H_2 – O_2 –Ar using intrinsic low-dimensional manifolds and wavelet adaptive multilevel representation

Sandeep Singh, Yevgenii Rastigejev, Samuel Paolucci and Joseph M Powers

Department of Aerospace and Mechanical Engineering, University of Notre Dame, Notre Dame, IN 46556-5637, USA

E-mail: ssingh@nd.edu, yrastige@nd.edu, paolucci@nd.edu and powers@nd.edu

Received 11 April 2000, in final form 15 February 2001

Abstract

A standard ignition delay problem for a mixture of hydrogen–oxygen–argon in a shock tube is extended to the viscous regime and solved using the method of intrinsic low-dimensional manifolds (ILDm) coupled with a wavelet adaptive multilevel representation (WAMR) spatial discretization technique. An operator-splitting method is used to describe the reactions as a system of ordinary differential equations at each spatial point. The ILDM method is used to eliminate the stiffness associated with the chemistry by decoupling processes which evolve on fast and slow time scales. The fast time scale processes are systematically equilibrated, thereby reducing the dimension of the phase space required to describe the reactive system. The WAMR technique captures the detailed spatial structures automatically with a small number of basis functions thereby further reducing the number of variables required to describe the system. A maximum of only 300 collocation points and 15 scale levels yields results with striking resolution of fine-scale viscous and induction zones. Additionally, the resolution of physical diffusion processes minimizes the effects of potentially reaction-inducing artificial entropy layers associated with numerical diffusion.

1. Introduction

We present results of the application of new algorithms for computing a standard problem in combustion. The intrinsic low-dimensional manifolds (ILDm) method, which rationally reduces detailed kinetic systems, and the wavelet adaptive multilevel representation (WAMR) technique, which allows for efficient resolution of detailed spatial structures, are brought together to address the problem of ignition delay in a shock tube filled with a mixture of hydrogen–oxygen–argon.

It is well known that in order to accurately simulate a wide variety of thermochemical phenomena, the effects of detailed finite-rate chemistry must be incorporated into models.

However, implementation of fully detailed chemistry models with the obligatory numerical resolution has proved to require a prohibitive amount of computational resources for all but the simplest of flows. While the addition of species and reaction mechanisms induces an increase in computational time required to simulate a given event, a more serious problem is often the severe stiffness associated with the differential equations which model the chemistry. In general, the time scales of the reaction are often widely disparate. This leads to computations which routinely take hundreds of hours on supercomputers; such efforts are often impractical. Consequently, it becomes necessary to implement a strategy to reduce the stiffness introduced by the chemistry. The simplest, full equilibrium, is effectively an ILDM of dimension zero; however, this approach will necessarily miss the coupling of events which occur at time scales of the chemical reaction. Simple and often useful strategies which capture some of the kinetic time scales employ explicit one-step models, e.g. Westbrook and Dryer [1] or Khokhlov *et al* [2]. Also useful are the commonly employed partial equilibrium and steady-state modelling assumptions.

As shown by Maas and Pope [3], such assumptions are often not robust. While they may be useful in the range in which they have been calibrated, it is easy to find scenarios where such models cannot accurately reproduce the results of full kinetic models. Consequently, Maas and Pope [3] and simultaneously Goussis and Lam [4] have advocated methods which systematically reduce chemical kinetic models in such a way that consistency with full model equations is maintained to a user-specified precision. A number of studies have appeared in recent years advancing the technique and some variants (cf Blasenbrey *et al* [5], Eggels *et al* [6], Hamiroune *et al* [7], Lam [8], Schmidt *et al* [9], Norris [10], Yang and Pope [11, 12] and Hadjinicolaou and Goussis [13]). In this study we have used the method of Maas and Pope, which systematically equilibrates the fast time scales and resolves the slow time scales of the reaction mechanism, thereby eliminating the associated stiffness. We cast our development of the ILDM method so that it is applicable under the rather general conditions which naturally arise from an operator-splitting method applied to fully compressible, non-adiabatic, non-isobaric, diffusive systems. Such conditions are not fully discussed in most of the ILDM literature and must be considered if the ILDM method is to be used for general problems.

Traditionally convection and diffusion in reactive flow problems are modelled by finite-difference or finite-element methods, which have difficulty modelling phenomena which have localization in physical and spectral space. Here we use a WAMR technique, which is better suited for problems with physical and spectral localization. This technique, developed by Vasilyev and Paolucci [14, 15], projects the representation of the system onto a wavelet basis. This basis has been shown to be very efficient in representing systems with detailed spatial structures. The capturing of the details of the structures with a small number of basis functions dramatically reduces the number of equations which need to be solved, consequently reducing the required computational time.

The ignition delay problem we consider is the viscous analogue of the inviscid problem considered by Fedkiw *et al* [16] (see also [17]) and is as follows. As an initial condition, a shock is taken to be propagating to the right in a mixture of hydrogen–oxygen–argon. The shock is of insufficient strength to induce significant reaction over the length scales considered. After some time, the shock reflects from the right wall, inducing a reflected, left-propagating shock. This shock leaves the fluid adjacent to the wall in a state of near zero velocity and a temperature which is sufficiently elevated to induce significant chemical reaction following a short ignition delay time. The problem considered in [16] is very similar to that studied by Oran *et al* [18], who, in a case they label ‘strong ignition’, consider the same gaseous mixture at a reflected shock pressure which is roughly 10% higher and a temperature which is roughly

10% lower than that considered in [16]. Additionally, there are small differences between the models used in [16, 18].

A Strang [19] operator-splitting technique is used in the numerical simulation of the governing equations. This technique allows straightforward implementation of both the ILDM and WAMR techniques. After initialization, the Strang-splitting progresses in a series of two-step processes. In the first step, convection and diffusion are suppressed. In this step, each point in space is treated as a homogeneous premixed reactor under constant density adiabatic conditions, and the associated ordinary differential equations at each point in space are solved using the ILDM method. In the second step, the reaction source terms are deactivated, the solution at each spatial point evolves due to convection and diffusion, and the associated partial differential equations are solved using the WAMR method.

While diffusion is typically not modelled in detonation studies, it is considered here for two reasons. First, as discussed in detail by Singh *et al* [20], physical diffusion is necessary to regularize predictions of flow variables downstream of the lead shock in simulations of multidimensional cellular instabilities. Whether or not this physically based regularization is crucial in determining wall tracings is an open question. Second, as will be shown here, the use of physical diffusion correctly captures entropy layers. As discussed by Menikoff [21], inviscid models using typical grid resolutions will introduce artificial entropy layers due to numerical diffusion. The coarser the grid, the more entropy introduced, and the more likely such a layer could falsely trigger a temperature-sensitive chemical reaction.

The paper is organized as follows. The governing equations, initial and boundary conditions are described first. Next, a detailed description of the operator-splitting technique is given along with a brief review of the WAMR technique. The ILDM method for a homogeneous premixed system is then discussed, and it is shown how it naturally can be used in an operator-splitting scheme to solve more general partial differential equations with convection and diffusion. Detailed results are given for the shock tube test problem, and conclusions are presented.

2. Governing equations

The following equations describe the system we consider, a one-dimensional viscous mixture of N ideal gases composed of L elements which undergo J reactions.

$$\frac{\partial \rho}{\partial t} + \frac{\partial}{\partial x} (\rho u) = 0 \quad (1)$$

$$\frac{\partial}{\partial t} (\rho u) + \frac{\partial}{\partial x} (\rho u^2 + p - \tau) = 0 \quad (2)$$

$$\frac{\partial}{\partial t} \left(\rho \left(e + \frac{u^2}{2} \right) \right) + \frac{\partial}{\partial x} \left(\rho u \left(e + \frac{u^2}{2} \right) + u (p - \tau) + J^q \right) = 0 \quad (3)$$

$$\frac{\partial}{\partial t} (\rho y_l) + \frac{\partial}{\partial x} (\rho u y_l + j_l) = 0 \quad (l = 1, \dots, L - 1) \quad (4)$$

$$\frac{\partial}{\partial t} (\rho Y_i) + \frac{\partial}{\partial x} (\rho u Y_i + J_i^m) = \dot{\omega}_i M_i \quad (i = 1, \dots, N - L) \quad (5)$$

$$\tau = \frac{4}{3} \mu \frac{\partial u}{\partial x} \quad (6)$$

$$J^q = -k \frac{\partial T}{\partial x} + \sum_{i=1}^N J_i^m \left(h_i^o + \int_{T_o}^T c_{pi}(\hat{T}) d\hat{T} \right) - \Re T \sum_{i=1}^N \frac{\mathcal{D}_i^T}{M_i} \left(\frac{1}{\chi_i} \frac{\partial \chi_i}{\partial x} + \left(1 - \frac{M_i}{M} \right) \frac{1}{p} \frac{\partial p}{\partial x} \right) \quad (7)$$

$$J_i^m = \rho \sum_{j=1, j \neq i}^N \frac{M_i}{M} Y_j \mathcal{D}_{ij} \left(\frac{1}{\chi_j} \frac{\partial \chi_j}{\partial x} + \left(1 - \frac{M_j}{M} \right) \frac{1}{p} \frac{\partial p}{\partial x} \right) - \mathcal{D}_i^T \frac{1}{T} \frac{\partial T}{\partial x} \quad (i = 1, \dots, N) \quad (8)$$

$$M = \sum_{i=1}^N M_i \chi_i \quad (9)$$

$$\chi_i = \frac{M}{M_i} Y_i \quad (i = 1, \dots, N) \quad (10)$$

$$y_l = m_l \sum_{i=1}^N \frac{\phi_{il}}{M_i} Y_i \quad (l = 1, \dots, L - 1) \quad (11)$$

$$j_l = m_l \sum_{i=1}^N \frac{\phi_{il}}{M_i} J_i^m \quad (l = 1, \dots, L - 1) \quad (12)$$

$$\sum_{i=1}^N Y_i = 1 \quad (13)$$

$$\sum_{l=1}^L y_l = 1 \quad (14)$$

$$\dot{\omega}_i = \sum_{j=1}^J a_j T^{\beta_j} \exp \left(\frac{-E_j}{\Re T} \right) (v_{ij}'' - v_{ij}') \prod_{k=1}^N \left(\frac{\rho Y_k}{M_k} \right)^{v_{kj}'} \quad (i = 1, \dots, N - L) \quad (15)$$

$$p = \frac{\rho \Re T}{M} \quad (16)$$

$$e = \sum_{i=1}^N Y_i \left(h_i^o + \int_{T_o}^T c_{pi}(\hat{T}) d\hat{T} \right) - \frac{\Re T}{M}. \quad (17)$$

Equations (1)–(4) describe the conservation of mass, linear momentum, energy and mass fraction of $L - 1$ elements. Equation (5) is an evolution equation for $N - L$ of the N species. Equations (6)–(8) give constitutive relations for momentum, energy and mass diffusion, which are the Newtonian stress–strain rate relation, extended Fourier’s law and extended Fick’s law. The form of both Fourier’s and Fick’s law given at this point are appropriate for a mixture of ideal gases, as detailed in a derivation by Merk [22] and summarized by Kee *et al* [23]. Equations (7) and (8) account for multicomponent mass diffusion as well as Soret and DuFour effects, all of which are included at this stage for completeness. We will later reduce this to a simpler form which we use in the analysis. Equation (9) defines the mean molecular mass, and equation (10) defines the species mole fraction. Equations (11) and (12) define the mass fraction and diffusive mass flux of element l . Equations (13) and (14) constrain the species and element mass fractions to sum to unity. Equation (15) is a constitutive equation for the evolution of species given by the law of mass action with Arrhenius kinetics. Equations (16) and (17) are, respectively, thermal and caloric state equations for a mixture of ideal gases with temperature-dependent specific heats.

The $N + 2$ partial differential equations (1)–(5) are taken to be fundamental equations for $N + 2$ dependent variables, which we take to be: the mass density, ρ ; the mass-averaged velocity, u ; the mass-averaged internal energy per unit mass, e ; the mass fraction of element l , y_l ($l = 1, \dots, L - 1$); and the mass fraction of species i , Y_i ($i = 1, \dots, N - L$). These are supplemented by $3N + L + 5$ constitutive equations, equations of state, and supplementary algebraic equations (6)–(17) for the remaining $3N + L + 5$ intermediate variables which we take to be: the pressure, p ; the viscous stress, τ ; the diffusive energy flux, J^q ; the mole fraction of species i , χ_i ($i = 1, \dots, N$); the mass fraction of element L , y_L ; the mass fraction of species i , Y_i ($i = N - L + 1, \dots, N$); the diffusive mass flux of element l , j_l ($l = 1, \dots, L - 1$); the diffusive mass flux of species i , J_i^m ($i = 1, \dots, N$); the molar production rate per unit volume of species i , $\dot{\omega}_i$ ($i = 1, \dots, N - L$); the mean molecular mass, M ; and the temperature, T . The independent variables are time t and position x . The specific heat of species i on a mass basis, c_{pi} , is taken to be a known function of temperature. The function is taken to be in the form of a standard polynomial curve fit found in the Chemkin III thermodynamic database [24].

Constant parameters in equations (1)–(17) are M_i , m_l , a_j , β_j , E_j , \mathfrak{R} , v'_{ij} , v''_{ij} , ϕ_{il} , \mathcal{D}_{ij} , \mathcal{D}_i^T , μ , k and h_i^o . They represent the molecular mass of species i , the atomic mass of element l , the kinetic rate constant of reaction j , the temperature dependence exponent of reaction j , the activation energy of reaction j , the universal gas constant ($\mathfrak{R} = 8.31441 \text{ J mol}^{-1} \text{ K}^{-1}$), the stoichiometric coefficient of the i th species in reaction j of the reactants and products, respectively, the number of atoms of element l in species i , the multicomponent mass diffusion coefficient, the Soret–DuFour thermal diffusion coefficient, the dynamic viscosity, the thermal conductivity and the standard enthalpy of formation per unit mass of species i . All reactions are treated as forward reactions with explicit reactions written for the actual reverse reactions. Following Maas and Warnatz [25], coefficients for those reactions which could be written as reverse reactions are chosen to be consistent with thermodynamic equilibrium relations.

Many studies do not explicitly form equation (4) and instead solve $N - 1$ species equations. Equation (4) is included because it is critical in the implementation of the ILDM method within an operator-splitting scheme. Equation (4), along with equations (1) and (13), can be obtained by enforcing stoichiometric balances for the j th reaction $\sum_{i=1}^N v'_{ij} \phi_{il} = \sum_{i=1}^N v''_{ij} \phi_{il}$ for $l = 1, \dots, L$, and the definition of the molecular mass, $M_i = \sum_{l=1}^L \phi_{il} m_l$, along with equation (11) and appropriate manipulations of equation (5) when written in a form in which the evolution of all N species is considered.

It is straightforward to show that conditions exist which guarantee a constant element mass fraction for all time. Using equation (1) and introducing the material derivative,

$$\frac{D}{Dt} \equiv \frac{\partial}{\partial t} + u \frac{\partial}{\partial x}$$

equation (4) transforms to

$$\rho \frac{Dy_l}{Dt} = - \frac{\partial j_l}{\partial x} \quad (l = 1, \dots, L - 1). \quad (18)$$

For general expressions of mass diffusion, such as that of equation (8), the right-hand side of equation (18) will be non-zero, and one can conclude that the element mass fraction of a fluid particle will change with time. Assuming now that: (a) all multicomponent mass diffusion coefficients are equal, $\mathcal{D}_{ij} = \mathcal{D}$; (b) the molecular masses of each species are close to the mean molecular mass, $M_i \sim M$, and consequently mass fractions are roughly the same as mole fractions $Y_i \sim \chi_i$; and (c) Soret mass diffusion due to thermal effects is negligible, $\mathcal{D}_i^T \sim 0$, and consequently DuFour effects are negligible as well, we arrive at a form of Fick's law

commonly used in the combustion community, e.g. Williams [26] and Merk [22], and which we adopt from here on

$$J_i^m = -\rho D \frac{\partial Y_i}{\partial x} \quad (i = 1, \dots, N). \quad (19)$$

We note that for our specific problem with the present reaction mechanism it can be shown, using a Maxwell diffusion formulation, that assumption (b) is not necessary.

Now using equation (19), equation (12) reduces, using equation (11), to

$$j_l = -\rho D \frac{\partial y_l}{\partial x} \quad (l = 1, \dots, L - 1). \quad (20)$$

Then equation (18) simplifies through use of equation (20) to

$$\rho \frac{Dy_l}{Dt} = D \frac{\partial}{\partial x} \left(\rho \frac{\partial y_l}{\partial x} \right) \quad (l = 1, \dots, L - 1). \quad (21)$$

Consequently, for a system with a diffusive mass flux of the described character, no initial gradients of element mass fraction $\frac{\partial y_l}{\partial x}(x, t = 0) = 0$, and no fluxes at boundaries $\frac{\partial y_l}{\partial x}(x = 0, t) = \frac{\partial y_l}{\partial x}(x = L_x, t) = 0$ (where L_x is the domain length), equations (21) and (14) ensure there is no tendency for any element mass fraction to change from its uniform initial value, and each element mass fraction will remain constant for all x and t . The same conclusion obviously holds for systems with no mass diffusion. For non-premixed flames with similar assumptions, the mixture fraction described by Warnatz *et al* [27] can be used to parametrize the y_l values in such a way that also simplifies the system.

We recognize that the assumptions necessary to obtain equation (21) are somewhat crude for our mixture, and note that this most likely induces small errors in zones in which mass fraction gradients are steep. While our method can deal with the more complete system, we have simplified it for the following two reasons: (a) if we allowed preferential diffusion, we would be obliged to use an ILDM of much higher dimension in order to account for local non-conservation of the element mass fraction and (b) while the computational cost for adding such terms would be high, it is not clear that the effect of those terms in this problem is large.

The kinetic model, identical to that used in [16], was originally developed by Maas and Warnatz [25] and considers the reaction of $N = 9$ species (H, O, H₂, O₂, OH, H₂O, HO₂, H₂O₂, Ar) constituted from $L = 3$ elements (H, O, Ar), in $J = 37$ reactions. Coefficients for this mechanism are listed in table 1. For this mechanism, we have adopted the corrected value of third-body efficiency for hydrogen, $f_{H_2} = 1.00$, as appears in [3]. As reported in [25], no special tuning was imposed to match experimentally observed ignition delay times.

In order to verify the kinetic model, preliminary calculations were performed to simulate the experiments of Schott and Kinsey [28]. In their experiments, induction times, t_i , were measured in shock tubes for dilute, low-pressure ($p \sim 30$ kPa) mixtures of H₂ and O₂ in Ar. The kinetic model under adiabatic, isochoric, homogeneous premixed conditions predicted induction times which were within the experimental error bounds reported for the conditions of [28]. A full simulation including the effect of spatial gradients proved impractical. This is because the instrumentation in the experiment required at least a 1 ms induction time, rendering the ratio of the induction time to the reaction time sufficiently large to make its computation with full spatial details prohibitively expensive. In order to match with [16], at the higher-pressure conditions we consider, in which the reflected shock pressure and temperature are 118.8 kPa and 1196 K, respectively, a homogeneous premixed, adiabatic, isochoric calculation with the kinetic model for $2H_2 + O_2 + 7Ar$ yields $t_i = 58.2 \mu s$. This is within the error bounds of an extrapolation of the results of [28], which predicts $7.3 < t_i < 81.9 \mu s$ at this state.

Table 1. Nine-species, 37-step reaction mechanism for a hydrogen–oxygen–argon mixture [25] with corrected f_{H_2} from [3], also utilized by Fedkiw *et al* [16]. Units of a_j are in appropriate combinations of cm, mol, s and K so that $\dot{\omega}_i$ has units of mol cm⁻³ s⁻¹; units of E_j are kJ mol⁻¹. Third-body collision efficiencies with M are $f_{\text{H}_2} = 1.00$, $f_{\text{O}_2} = 0.35$ and $f_{\text{H}_2\text{O}} = 6.5$.

j	Reaction	a_j	β_j	E_j
1	O ₂ + H → OH + O	2.00 × 10 ¹⁴	0.00	70.30
2	OH + O → O ₂ + H	1.46 × 10 ¹³	0.00	2.08
3	H ₂ + O → OH + H	5.06 × 10 ⁴	2.67	26.30
4	OH + H → H ₂ + O	2.24 × 10 ⁴	2.67	18.40
5	H ₂ + OH → H ₂ O + H	1.00 × 10 ⁸	1.60	13.80
6	H ₂ O + H → H ₂ + OH	4.45 × 10 ⁸	1.60	77.13
7	OH + OH → H ₂ O + O	1.50 × 10 ⁹	1.14	0.42
8	H ₂ O + O → OH + OH	1.51 × 10 ¹⁰	1.14	71.64
9	H + H + M → H ₂ + M	1.80 × 10 ¹⁸	-1.00	0.00
10	H ₂ + M → H + H + M	6.99 × 10 ¹⁸	-1.00	436.08
11	H + OH + M → H ₂ O + M	2.20 × 10 ²²	-2.00	0.00
12	H ₂ O + M → H + OH + M	3.80 × 10 ²³	-2.00	499.41
13	O + O + M → O ₂ + M	2.90 × 10 ¹⁷	-1.00	0.00
14	O ₂ + M → O + O + M	6.81 × 10 ¹⁸	-1.00	496.41
15	H + O ₂ + M → HO ₂ + M	2.30 × 10 ¹⁸	-0.80	0.00
16	HO ₂ + M → H + O ₂ + M	3.26 × 10 ¹⁸	-0.80	195.88
17	HO ₂ + H → OH + OH	1.50 × 10 ¹⁴	0.00	4.20
18	OH + OH → HO ₂ + H	1.33 × 10 ¹³	0.00	168.30
19	HO ₂ + H → H ₂ + O ₂	2.50 × 10 ¹³	0.00	2.90
20	H ₂ + O ₂ → HO ₂ + H	6.84 × 10 ¹³	0.00	243.10
21	HO ₂ + H → H ₂ O + O	3.00 × 10 ¹³	0.00	7.20
22	H ₂ O + O → HO ₂ + H	2.67 × 10 ¹³	0.00	242.52
23	HO ₂ + O → OH + O ₂	1.80 × 10 ¹³	0.00	-1.70
24	OH + O ₂ → HO ₂ + O	2.18 × 10 ¹³	0.00	230.61
25	HO ₂ + OH → H ₂ O + O ₂	6.00 × 10 ¹³	0.00	0.00
26	H ₂ O + O ₂ → HO ₂ + OH	7.31 × 10 ¹⁴	0.00	303.53
27	HO ₂ + HO ₂ → H ₂ O ₂ + O ₂	2.50 × 10 ¹¹	0.00	-5.20
28	OH + OH + M → H ₂ O ₂ + M	3.25 × 10 ²²	-2.00	0.00
29	H ₂ O ₂ + M → OH + OH + M	2.10 × 10 ²⁴	-2.00	206.80
30	H ₂ O ₂ + H → H ₂ + HO ₂	1.70 × 10 ¹²	0.00	15.70
31	H ₂ + HO ₂ → H ₂ O ₂ + H	1.15 × 10 ¹²	0.00	80.88
32	H ₂ O ₂ + H → H ₂ O + OH	1.00 × 10 ¹³	0.00	15.00
33	H ₂ O + OH → H ₂ O ₂ + H	2.67 × 10 ¹²	0.00	307.51
34	H ₂ O ₂ + O → OH + HO ₂	2.80 × 10 ¹³	0.00	26.80
35	OH + HO ₂ → H ₂ O ₂ + O	8.40 × 10 ¹²	0.00	84.09
36	H ₂ O ₂ + OH → H ₂ O + HO ₂	5.40 × 10 ¹²	0.00	4.20
37	H ₂ O + HO ₂ → H ₂ O ₂ + OH	1.63 × 10 ¹³	0.00	132.71

We take $\mathcal{D} = 5.6 \times 10^{-3} \text{ m}^2 \text{ s}^{-1}$, $\mu = 1.0 \times 10^{-3} \text{ N s m}^{-2}$ and $k = 8.3 \times 10^0 \text{ W m}^{-1} \text{ K}^{-1}$. We note that the viscosity is roughly one order of magnitude too large. Computations with a viscosity of the right magnitude would entail a much higher computational cost. There are two reasons for taking the larger value of viscosity. First, since our wavelet approach will capture all length scales present, four more wavelet levels would be required for the smaller viscosity. In addition to an increase in the number of degrees of freedom, this would require roughly an order of magnitude reduction in the time step. Second, subsequent calculations using 19 dyadic levels of resolution (from laboratory scale to viscous scale) would necessitate

quadruple-precision computations because approximations of second derivatives on the finest scale using double precision are corrupted by machine roundoff! A discussion of the effect of our choice of viscosity on the results is given later.

We consider a shock tube of length 0.12 m filled initially with H₂, O₂ and Ar in a 2:1:7 molar ratio. For $0 \leq x \leq 0.06$ m, the gas is taken to be at $\rho = 0.18075 \text{ kg m}^{-3}$, $u = 487.34 \text{ m s}^{-1}$ and $p = 35.594 \text{ kPa}$. For $0.06 < x \leq 0.12$ m, the gas is at $\rho = 0.072 \text{ kg m}^{-3}$, $u = 0 \text{ m s}^{-1}$ and $p = 7.173 \text{ kPa}$. This state is consistent with Rankine–Hugoniot jump conditions for the inviscid equivalent of equations (1)–(17). Knowledge of these parameters allows determination of all other dependent variables at $t = 0$ s through the use of the governing equations. At $x = 0.12$ m, we consider a boundary which is closed and adiabatic. Consequently, $u = 0 \text{ m s}^{-1}$, and additionally diffusive mass and energy fluxes J_i^m ($i = 1, \dots, N$), and J^q must be zero. At $x = 0$ m, we allow inflow conditions of $u = 487.34 \text{ m s}^{-1}$, $\rho = 0.18075 \text{ kg m}^{-3}$, $p = 35.594 \text{ kPa}$.

3. Operator splitting

The governing equations (1)–(17) can be written in the following compact form:

$$\frac{\partial \mathbf{x}}{\partial t} = \mathbf{F}(\mathbf{x}) - \frac{\partial}{\partial x} \mathbf{\Pi}(\mathbf{x}) \quad (22)$$

where \mathbf{x} , representing a set of conserved dependent variables, $\mathbf{F}(\mathbf{x})$, representing a reaction source term, and $-\frac{\partial}{\partial x} \mathbf{\Pi}(\mathbf{x})$ representing convection and diffusion, are given by

$$\mathbf{x} = \begin{pmatrix} \rho \\ \rho u \\ \rho \left(e + \frac{1}{2} (u^2) \right) \\ \rho y_1 \\ \vdots \\ \rho y_{L-1} \\ \rho Y_1 \\ \vdots \\ \rho Y_{N-L} \end{pmatrix} \quad \mathbf{F}(\mathbf{x}) = \begin{pmatrix} 0 \\ 0 \\ 0 \\ 0 \\ \vdots \\ 0 \\ \dot{\omega}_1 M_1 \\ \vdots \\ \dot{\omega}_{N-L} M_{N-L} \end{pmatrix} \quad (23)$$

$$\mathbf{\Pi}(\mathbf{x}) = \begin{pmatrix} \rho u \\ \rho u^2 + p - \tau \\ \rho u \left(e + \frac{1}{2} (u^2) \right) + u (p - \tau) + J^q \\ \rho u y_1 + j_1 \\ \vdots \\ \rho u y_{L-1} + j_{L-1} \\ \rho u Y_1 + J_1^m \\ \vdots \\ \rho u Y_{N-L} + J_{N-L}^m \end{pmatrix}.$$

Here \mathbf{x} , \mathbf{F} and $\mathbf{\Pi}$ are all of length $N+2$. Equation (22) is solved in two steps, a reaction step and a convection–diffusion step, using Strang-splitting [19]. This splitting results in second-order accuracy in time.

3.1. Reaction step

In step 1, the following equation, equivalent to that for a homogeneous premixed reactor at every point in the space, is solved at each spatial point:

$$\frac{\partial \mathbf{x}}{\partial t} = \mathbf{F}(\mathbf{x}). \quad (24)$$

The first $2 + L$ equations of equation (24) are homogeneous and can be integrated exactly to give

$$\rho = \rho_o \quad u = u_o \quad e = e_o \quad y_l = y_{l_o} \quad (l = 1, \dots, L - 1). \quad (25)$$

Hence, the $N - L$ species evolution equations in equation (24) reduce to the following partial differential equations, which are treated at each point in space as ordinary differential equations with ρ, u, e and y_l held constant to the values given in equation (25) every time step 1 is repeated:

$$\frac{\partial Y_i}{\partial t} = \frac{\dot{\omega}_i M_i}{\rho_o} \quad (i = 1, \dots, N - L). \quad (26)$$

It is noted that while during a single time step the values of ρ_o, e_o, u_o and y_{l_o} do not change; because of convection and diffusion, in general, all will change with time.

In the next section we discuss how $\dot{\omega}_i$ can be cast in terms of Y_i for $i = 1, \dots, N - L$; thus, equation (26) is well posed and can be solved in its entirety by any standard implicit or explicit technique at every point in space. Because the equations are stiff, we use the LSODE software package [29] in full implicit mode when solving the full set of equation (26). Alternatively, equation (26) can be solved using the ILDM method, described in a following section, which systematically removes the stiffness associated with reactions. When using the ILDM method, we use a simpler explicit Runge–Kutta method for time advancement, which is second-order accurate in time. The size of the time step is dictated by the convection–diffusion time step restriction discussed in the next section.

3.2. Convection–diffusion step

In step 2, the following equation, which is a set of partial differential equations, is solved for the convection diffusion step:

$$\frac{\partial \mathbf{x}}{\partial t} = -\frac{\partial}{\partial x} \mathbf{\Pi}(\mathbf{x}). \quad (27)$$

Again, equation (27) can be solved by a variety of standard discretization techniques developed for inert fluid mechanics. Here we use the WAMR technique, as discussed in detail by Vasilyev and Paolucci [14, 15]. The method is summarized as follows. At any given time step, the pressure, temperature, density and velocity fields are projected onto a multilevel wavelet basis. The amplitudes of the wavelet basis functions give a measure of the importance of a particular wavelet mode. Additionally, one has available *a priori* error estimates, in contrast to most gradient-based adaptive mesh refinement techniques. All wavelets whose amplitude are below a defined threshold are removed. Calculations are performed for each wavelet whose amplitude is above the threshold (essential wavelets) and for a certain number below the threshold (neighbouring wavelets). If at the completion of a time step, an essential wavelet has its amplitude drop below the threshold, it is reclassified as a neighbouring wavelet or eliminated, and the neighbouring region is adjusted; similarly, if a wavelet in the neighbouring region has its amplitude become sufficiently large, it is reclassified as an essential wavelet, and the neighbouring region is adjusted. The method is based on a collocation strategy using the

autocorrelation function of the Daubechies scaling function of the order of four as the basis. A linearized trapezoidal (implicit) scheme in conjunction with GMRES iterations is used for time advancement. The size of the time step is chosen to satisfy a CFL condition associated with the fastest local velocity.

4. ILDM for a homogeneous premixed reactive system

In the operator-splitting technique which is employed to solve equation (22), each discrete point in space behaves as an adiabatic, homogeneous premixed reactor, thus enabling the use of the ILDM technique. The method provides a systematic way to overcome the severe stiffness which is associated with full models of gas phase combustion, and thus significantly improves computational efficiency. In a homogeneous premixed calculation, the full hydrogen–oxygen–argon model predicts the ratio of the time scale of the slowest reaction mode to that of the fastest reaction mode to typically reach values near 10^5 , which indicates severe stiffness is present. The ILDM method systematically eliminates most of this stiffness by equilibrating fast time scale events and describing parametrically a low-dimensional manifold upon which slow time scale events evolve.

Here, the method of Maas and Pope [3], slightly adapted for our system, is summarized. The constant density, isochoric, adiabatic combustion of a homogeneous premixed system of N species constituted from L elements can be expressed as $N - L$ nonlinear ordinary differential equations, which evolve in an $(N - L)$ -dimensional composition (phase) space:

$$\frac{dY_i}{dt} = \frac{\dot{\omega}_i M_i}{\rho_o} \quad (i = 1, \dots, N - L). \quad (28)$$

The specific internal energy of each component, e_i , is at most a function of temperature. The conditions under which equation (28) holds are identical to those employed in the operator splitting used to generate equation (26) and they can be solved in the same manner. Hence, equations (13) and (25) with (11) are appropriate to determine the remaining L mass fractions. For gases in the mixture that are thermally perfect, the specific internal energy of each component is at most a function of temperature. Hence, knowledge of the mass fractions and mass-averaged specific internal energy e_o allows one to use Newton's method to invert equation (17) to form $T = T(Y_1, \dots, Y_{N-L}; e_o, y_{1o}, \dots, y_{(L-1)o})$. Hence, $\dot{\omega}_i$, which is in general a function of temperature, density and species mass fractions, can now be considered as a function of only $N - L$ of the species mass fractions for fixed values of e_o , ρ_o and y_{1o} :

$$\dot{\omega}_i = \dot{\omega}_i(Y_1, \dots, Y_{N-L}; e_o, \rho_o, y_{1o}, \dots, y_{(L-1)o}) \quad i = 1, \dots, N - L. \quad (29)$$

Both $\dot{\omega}_i$ and e_i can be easily evaluated using the Chemkin III [30] package.

At fixed e_o , ρ_o and y_{1o} , equation (28) can be rewritten as

$$\frac{d\mathbf{Y}}{dt} = \mathbf{F}(\mathbf{Y}) \quad (30)$$

where $\mathbf{Y} = (Y_1, \dots, Y_{N-L})^T$ and

$$\mathbf{F}(\mathbf{Y}) = \left(\frac{\dot{\omega}_1 M_1}{\rho_o}, \dots, \frac{\dot{\omega}_{N-L} M_{N-L}}{\rho_o} \right).$$

The reciprocals of the eigenvalues of the Jacobian \mathbf{F}_Y at any point in the composition space identify the $N - L$ associated characteristic time scales. The corresponding eigenvectors identify the directions in which each eigenmode of the total trajectory evolves in composition

space. The ILDM is identified as a set of points in the composition space where the composition space velocity vector \mathbf{F} is orthogonal to the eigenvectors associated with fast time scales.

We outline here the analysis to compute the ILDM given in detail for a similar system first by Maas and Pope [3] and later extended by Maas [31] following the general theory given by Golub and Van Loan [32]. We choose to resolve M slow time scales; this will result in the choice of M species which will form part of the parametrization for the complete ILDM. This is formed via the following steps. First, we decompose the Jacobian matrix \mathbf{F}_Y with a real Schur decomposition:

$$\mathbf{F}_Y = \mathbf{Q} \cdot \mathbf{U} \cdot \mathbf{Q}^T \quad (31)$$

where \mathbf{Q} is the $(N - L) \times (N - L)$ orthogonal matrix of real Schur vectors and \mathbf{U} is an $(N - L) \times (N - L)$ upper-triangular matrix with eigenvalues along the main diagonal. Typically most eigenvalues are negative and real; for closed adiabatic systems near equilibrium, there is a guarantee of real negative eigenvalues. The matrix is ordered so that proceeding down the diagonal, the real part of the eigenvalue becomes progressively more negative. Thus, the eigenvalue at the bottom right is associated with the fastest stable mode.

The above Schur decomposition, combined with the solution of a Sylvester equation, allows the Jacobian to be written in the following form:

$$\mathbf{F}_Y = (\mathbf{Z}_S \quad \mathbf{Z}_F) \begin{pmatrix} \mathbf{N}_S & 0 \\ 0 & \mathbf{N}_F \end{pmatrix} \begin{pmatrix} \hat{\mathbf{Z}}_S \\ \hat{\mathbf{Z}}_F \end{pmatrix} \quad \text{with} \quad \begin{pmatrix} \hat{\mathbf{Z}}_S \\ \hat{\mathbf{Z}}_F \end{pmatrix} = (\mathbf{Z}_S \quad \mathbf{Z}_F)^{-1}. \quad (32)$$

Here \mathbf{Z}_S has M column vectors, each of length $N - L$, which span the subspace associated with the M slow time scales. Furthermore, \mathbf{Z}_F has $N - L - M$ column vectors, each of length $N - L$, which span the subspace associated with the $N - L - M$ fast time scales. The matrices $\hat{\mathbf{Z}}_S$ and $\hat{\mathbf{Z}}_F$ are as defined in equation (32), have dimension $M \times (N - L)$ and $(N - L - M) \times (N - L)$, respectively, and are associated with the reciprocal slow and fast basis vectors. The matrix \mathbf{N}_S has dimension $M \times M$, is upper-triangular, and has as its eigenvalues those associated with the slow time scales. The matrix \mathbf{N}_F has dimension $(N - L - M) \times (N - L - M)$, is upper-triangular, and has as its eigenvalues those associated with the fast time scales.

For fixed energy, density and element mass fractions, the ILDM method identifies M -dimensional subspaces ($M < N - L$) on which slower time scale events evolve. An ILDM which equilibrates the $N - L - M$ fast time scales and consequently describes the M -dimensional manifold is given by

$$\hat{\mathbf{Z}}_F \cdot \mathbf{F}(\mathbf{Y}) = 0 \quad (33)$$

which forms $N - L - M$ algebraic equations. For what is effectively a complicated one-step chemistry, we take $M = 1$.

To construct the manifold for fixed energy, density, and element mass fractions, one first determines the equilibrium point of the system, which is taken as the original seed value. In subsequent calculations, the most recently calculated point is used as the seed value. One then performs the local fast and slow subspace decomposition, which gives local eigenvalues and associated basis vectors for a system linearized about the seed value. One then perturbs $N - L$ of the species away from their seed values in a prescribed manner to form the M algebraic equations below:

$$\mathbf{P} \cdot (\mathbf{Y} - \mathbf{Y}_o) = \delta. \quad (34)$$

Here \mathbf{P} is a user-specified parametrization matrix of dimension $M \times (N - L)$, δ is a vector of length M which contains a user-specified increment in the projected mass fractions, and \mathbf{Y}_o is a vector of length $N - L$ which contains the seed values of mass fractions. These M

equations are solved simultaneously with the $N - L - M$ algebraic ILDM equations (33) with a predictor–corrector technique which uses a tangent predictor and a Newton’s method corrector to obtain the mass fractions at a new point on the manifold. The process is repeated to construct the global ILDM. We adapt the parametrization matrix \mathbf{P} to overcome difficulties associated with turning points of the manifold in composition space. The choice of \mathbf{P} is based on a continuation method which is an extrapolation of previous points of the ILDM used to estimate the location of the new points. This method can also be used for computing manifolds for an adiabatic, isobaric system.

With this analysis, an M -dimensional manifold can be identified in an $(N - L)$ -dimensional composition space for a given set of $\rho_o, e_o, y_{1_o}, \dots, y_{(L-1)_o}$. These are the ILDMs that are traditionally discussed in the literature. Thus, a different ILDM is required for a different set of densities, internal energies and element mass fractions. Since in general calculations one can expect all of these quantities to vary, the actual relevant reaction manifold which must be formed has dimension $K = M + 1 + L$ and can be tabulated numerically to give

$$Y_i = Y_i(Y_1, \dots, Y_M, e, \rho, y_1, \dots, y_{L-1}) \quad \text{for } i = M + 1, \dots, N - L \quad (35)$$

where Y_1, \dots, Y_M are the chosen reference variables for the ILDM lookup table. The reference variables are chosen in such a way that the ILDM is single valued with respect to these variables for easy lookup. While there is no guarantee of single-valuedness, in the problems studied, we have found it to be the case.

It is the dimension of the lookup table, K , which is critically important in manifold methods. Many previously reported calculations have been restricted to premixed conditions in the isobaric and/or adiabatic limits, thus reducing the dimension K . In the calculations presented here, variable energy and density are intrinsic features of the flow; given that we have chosen $M = 1$ and for the hydrogen–oxygen–argon system, $L = 3$, we, in principle, must deal with a table which has dimension $K = 5$. Because we study a uniformly premixed mixture, and because we have employed the earlier-described simplified diffusion model, $L - 1 = 2$ independent element mass fractions remain constant throughout the calculations at $y_{\text{H}} = 0.01277$, $y_{\text{O}} = 0.10137$, reducing the effective dimension of the manifold to $K = 3$; the variables of manifold parametrization are chosen to be e, ρ and $Y_{\text{H}_2\text{O}}$.

With $M = 1$, a projection of the ILDM for fixed internal energy, density (as well as the always fixed element mass fractions), for the hydrogen–oxygen–argon system is plotted in figure 1 with $Y_{\text{H}_2\text{O}}$ used as the reference-independent variable for the ILDM and $Y_{\text{H}_2\text{O}_2}$ as the dependent variable. Mass fractions for all species, not shown here, are also available as functions of $Y_{\text{H}_2\text{O}}$ for the same fixed internal energy and density. Also shown on the plot are projections of trajectories in this two-dimensional subspace for a variety of initial conditions. It is seen that all trajectories relax to the ILDM. As indicated in figure 1, the relaxation from the initial state to the manifold occurs on a relatively fast time scale on the order of microseconds, while once on the ILDM, the subsequent relaxation to final equilibrium occurs on a much slower time scale which is of the order of 0.1 ms. The phase trajectories appear to cross, but this is because they have been projected into a lower-dimensional space.

A projection of the $K = 3$ ILDM for constant density and the same constant element mass fractions for the hydrogen–oxygen–argon system is plotted in figure 2, with $Y_{\text{H}_2\text{O}}$ and e used as the reference-independent variables and $Y_{\text{H}_2\text{O}_2}$ as the dependent variable. The portion of the ILDM depicted closely corresponds to values realized in the detonation calculation. Also, for the system studied here, the dependence of all variables on density was weak for the range of realized density values.

Equation (30) can be solved using the ILDM method if the composition of the mixture at a given spatial point is close to the ILDM. One illustrative way to achieve this is to locally

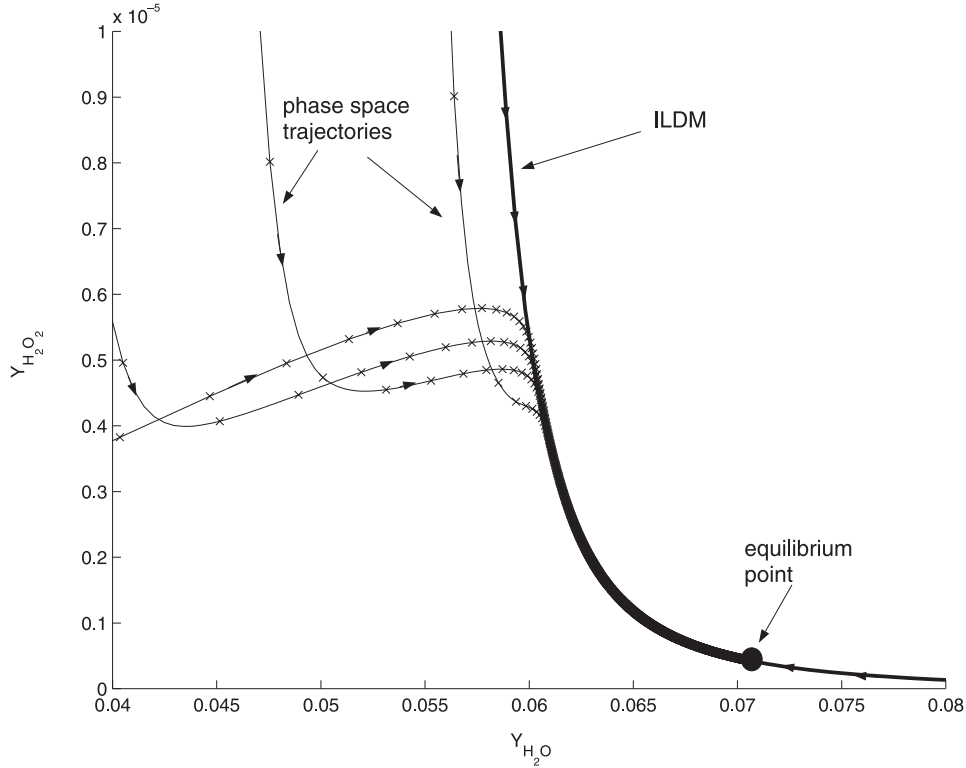


Figure 1. ILDM projection for the nine-species 37-step reaction mechanism of hydrogen–oxygen–argon combustion as a function of $Y_{\text{H}_2\text{O}}$ at constant values of $\rho = 0.5 \text{ kg m}^{-3}$, $e = 8.0 \times 10^3 \text{ J kg}^{-1}$. Element mass fractions fixed at $y_{\text{H}} = 0.01277$, $y_{\text{O}} = 0.10137$, $y_{\text{Ar}} = 0.88586$. Also plotted are trajectories from full time integration showing relaxation to the manifold and equilibrium. The symbol ‘x’ denotes equally spaced $0.10 \mu\text{s}$ time intervals. Total time to relax to equilibrium is near 0.1 ms .

project equation (30) onto the slow subspace:

$$\frac{d}{dt}(\hat{\mathbf{Z}}_S \cdot \mathbf{Y}) = \hat{\mathbf{Z}}_S \cdot \mathbf{F}(\mathbf{Y}). \quad (36)$$

This results in M ordinary differential equations and models the dynamics of reduced chemistry. In practice, we simply integrate M of the species equations (5) in their original form, while using the manifold to obtain all necessary secondary variables.

When using ILDMs with $M = 1$, we need to integrate only one differential equation associated with the reference variable at each spatial location. If the composition is far from the ILDM, it is important to incorporate the off-manifold kinetics in some fashion. Here the full reaction kinetic equations are integrated using LSODE in implicit mode. The integration is switched from full integration to the ILDM method when the L_2 norm between the actual mass fractions at a particular location and the corresponding projected mass fractions is less than 1×10^{-6} . While this reduces the efficacy of the ILDM method, it is critical to avoid large phase errors associated with projecting onto the manifold from a remote region of phase space. In other words, while all processes are typically destined to reach the manifold, it is critical for the proper sequencing of events that they reach the manifold at the correct time, and reach the right point on the manifold. A naive projection can easily give plausible answers which have

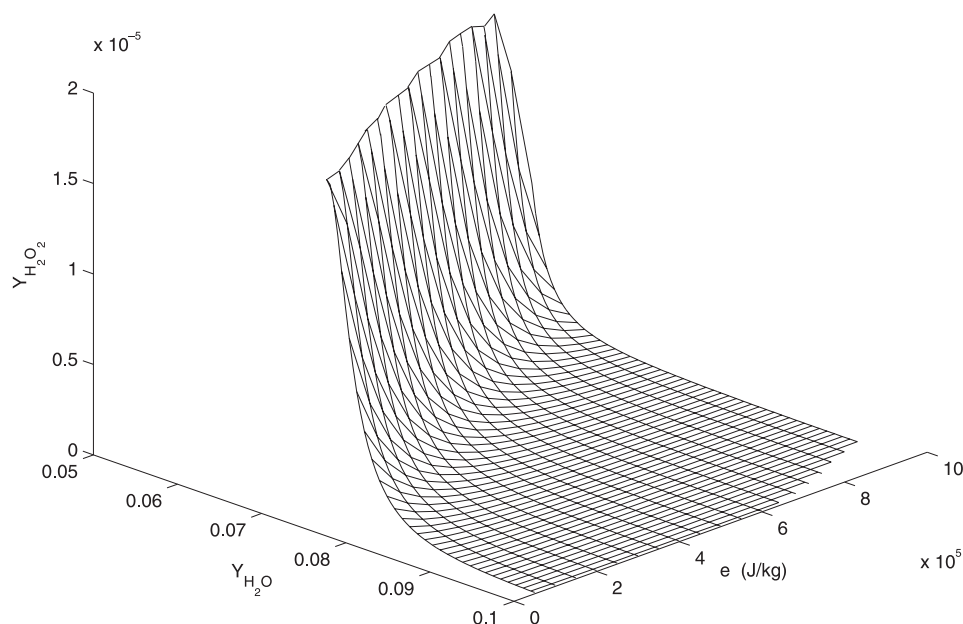


Figure 2. ILDM projection for the nine-species 37-step mechanism of hydrogen–oxygen–argon combustion giving $Y_{\text{H}_2\text{O}_2}$ as a function of $Y_{\text{H}_2\text{O}}$ and e for constant $\rho = 0.5 \text{ kg m}^{-3}$. Element mass fractions fixed at $y_{\text{H}} = 0.01277$, $y_{\text{O}} = 0.10137$, $y_{\text{Ar}} = 0.88586$.

$O(1)$ errors associated with them. In practice, in our calculations, we find we are able to use the ILDM method in cells which have recently been shocked, have passed through the bulk of the induction zone, and are well within the thermal explosion region. The ILDM method is also applied to points in the trailing rarefaction wave.

The convection–diffusion step is equivalent to a perturbation off the ILDM. Subsequent to the perturbation, there is a fast relaxation to the manifold corresponding to a new set of conserved variables. This is accomplished here by projection onto the manifold while holding the reference variable, here $Y_{\text{H}_2\text{O}}$, constant. This projection is allowed by the large time scale difference between slow chemical–fluid time scales and fast chemical time scales as long as convective and diffusive effects are not large. We also note that for this combustion mechanism the fast directions are nearly orthogonal to the slow variable, $Y_{\text{H}_2\text{O}}$, on the ILDM. Figure 3 depicts how this projection is accomplished. A slightly more accurate alternative would be to project on to the manifold in the direction of the vectors associated with the fast eigenmodes. In contrast to many implementations of the ILDM method for partial differential equations, which are often confined to a single adiabatic, isobaric ILDM, we convect and diffuse all variables, not just slow variables associated with the ILDM. While this comes at a cost of solving more equations, it is necessary to preserve the consistency of the Strang operator-splitting method. Alternatively, for our problem, which is neither adiabatic, isobaric or isochoric, we could choose to incur the extra expense of tabulating the slow and fast subspaces associated with changes in energy and density and then convect and diffuse just slow variables.

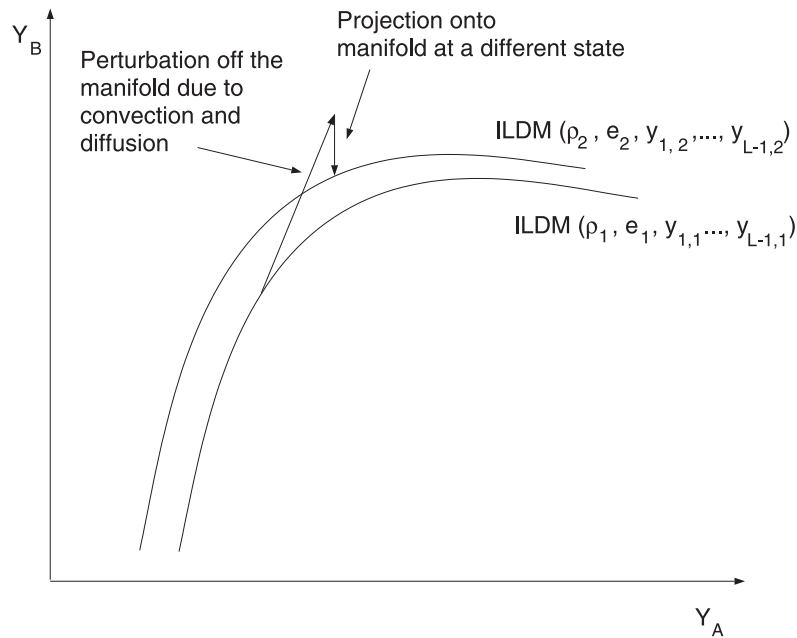


Figure 3. Sketch of projection to manifold of new energy and density levels following perturbation due to convection and diffusion.

5. Results

Results for the shock tube calculations are given here. Figure 4 gives predictions of temperature, velocity, pressure and density versus distance at time $t = 195 \mu\text{s}$. At this time, the lead right-travelling inert shock has reflected off the right wall and is propagating to the left with its head near $x = 0.065 \text{ m}$ at a pressure and temperature of 118.8 kPa and 1196 K, respectively. Close behind the lead shock is the much stronger, left-propagating Zeldovich–von Neumann–Doering (ZND) detonation wave, with its head near $x = 0.072 \text{ m}$. All of the usual salient features of a ZND detonation are predicted here. The von Neumann spike is predicted at a pressure of around 450 kPa, and the pressure relaxes to near 200 kPa at the right-hand boundary. The post-detonation temperatures are near 2500 K, and the velocity is seen to relax to a value of zero at the right-hand boundary.

The full curves show the predictions of the full chemical kinetics model. The dots show the results of the calculations using the ILDM resolving one reaction time scale; this can be interpreted as one-step chemistry with a rational fidelity to full chemical kinetics. It is seen on this scale that the predictions are nearly identical. Examination of the local eigenvalues indicates that use of the manifold suppresses temporal resolution of reaction events which occur faster than a roughly $0.1 \mu\text{s}$ time scale. For a given ρ and e , we construct the ILDM using adaptive parametrization as described by Maas [31]. This is done for 16 values of ρ ranging from 0.25 to 1.00 kg m^{-3} in steps of 0.05 kg m^{-3} . Similarly, we use 19 values of e ranging from 0.5×10^5 to $9.5 \times 10^5 \text{ J kg}^{-1}$ in steps of $0.5 \times 10^5 \text{ J kg}^{-1}$. Hence 304 slices such as shown in figure 1 were constructed. Finally, each ILDM was stored with an equally spaced parametrization of 100 values of $Y_{\text{H}_2\text{O}}$ for easy lookup. Thus, the ILDM lookup table has a size of $16 \times 19 \times 100$. For easy lookup, we have made use of a uniform grid.

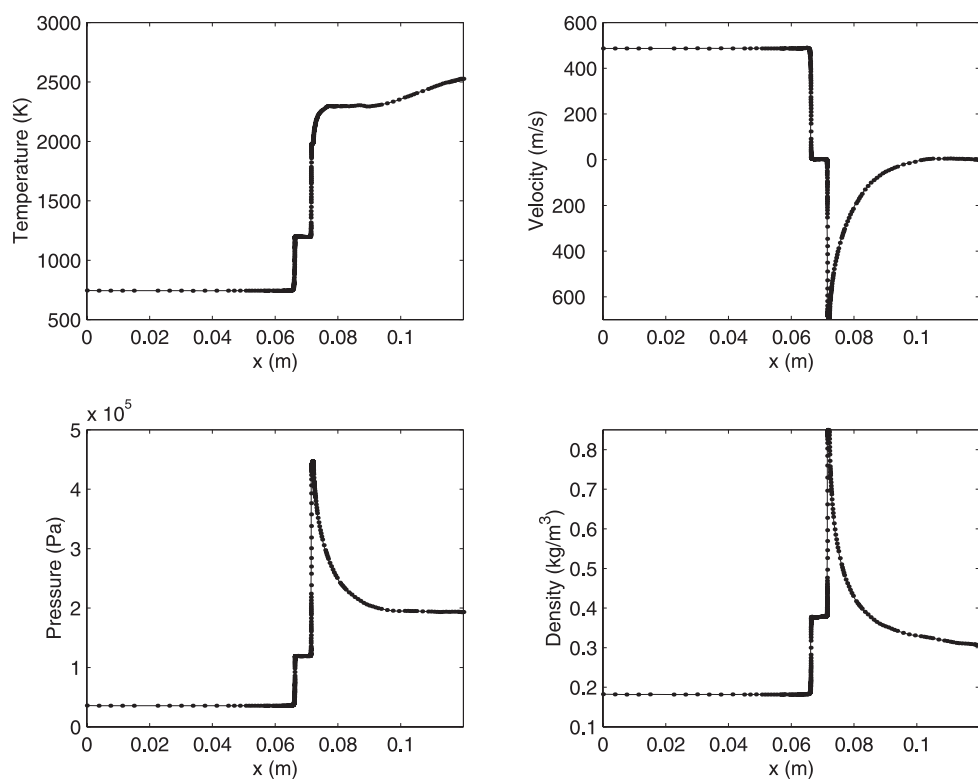


Figure 4. Predictions of temperature, velocity, pressure, and density versus distance at $t = 195 \mu\text{s}$ using a maximum of 300 collocation points, 15 scale levels for full chemical kinetics (full curves) and ILDM kinetics (dots) for viscous hydrogen–oxygen–argon detonation.

For this particular problem, use of the full integration technique requires three times as much computational time as the ILDM technique. We note, however, that general conclusions regarding computational efficiency are difficult to draw as the savings realized will be model-dependent as well as initial-condition-dependent. The bulk of our savings are realized near the end of the computation as more and more cells have become chemically activated. At the beginning of the calculation, when most cells are in a cold state far from equilibrium, there are no savings. The calculation itself took roughly 10 h on a 330 MHz Sun Ultra10 workstation.

Figure 5 shows similar results for the species mass fractions at the same time, $t = 195 \mu\text{s}$. Steep gradients in mass fractions are predicted near the detonation front. As expected, HO_2 , H and H_2O_2 mass fractions have relatively small values which peak at the detonation front. Under these conditions, the major product is H_2O . On the length scales shown in figures 4 and 5, the results appear to be very similar to the inviscid predictions of Fedkiw *et al* [16].

Figure 6 demonstrates the adaptive nature of the WAMR technique. It shows the distribution of collocation points and their scale levels, 2^{-j} , $j = 0, \dots, 14$, at two different times, first at $t = 180 \mu\text{s}$, when the lead shock and the approaching detonation are present, and later at $t = 230 \mu\text{s}$, after they have merged. In both cases, at most 300 collocation points and 15 wavelet scale levels were sufficient to capture the flow features to the prescribed dimensionless error tolerance of 10^{-3} . Moreover, it is clear that the algorithm adapts to the features of the flow.

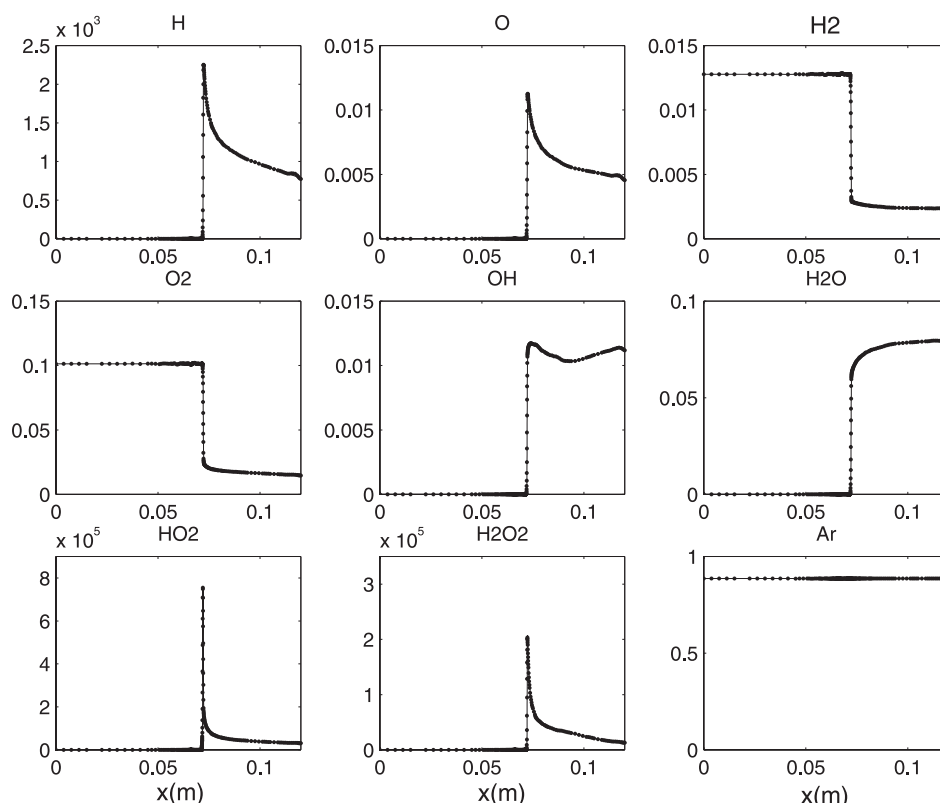


Figure 5. Predictions of species mass fractions versus distance at $t = 195 \mu\text{s}$ using a maximum of 300 collocation points, 15 scale levels for full chemical kinetics (full curves) and ILDM kinetics (dots) for viscous hydrogen–oxygen–argon detonation.

The effects of diffusion are clearly seen when one examines finer length scales. Figure 7 shows two views of pressure versus distance at a somewhat later time, $t = 230 \mu\text{s}$, by which time the detonation wave has overtaken the reflected shock. In the view on the left, the same length scale is shown as in figure 4. The view on the right shows a 120 factor spatial magnification near the lead shock. In this figure the dots represent the actual collocation points as chosen by the WAMR technique. It is clear on this scale that both the viscous shock and chemical induction zones have been resolved. Here it is predicted that the shock is essentially inert and has a thickness of roughly $50 \mu\text{m}$.

The induction zone, a region of essentially constant pressure, temperature and density, has a thickness of roughly $470 \mu\text{m}$. In the induction zone many reactions are occurring, giving rise to a release of energy which, because of the extreme temperature sensitivity of reaction rates, accumulates to an extent that a thermal explosion occurs at the end of the induction zone. While the wavelet representation certainly has captured these thin layers, it is noted that because it was chosen not to use individual species mass fractions as part of the adaption criteria, some finer scale reaction zone structures have not been spatially resolved.

In the process of understanding the time scales associated with the kinetics of a spatially homogeneous mixture, we have computed all time scales through an eigenvalue analysis. This analysis indicates that reaction time scales as small as sub-nanosecond are predicted by the

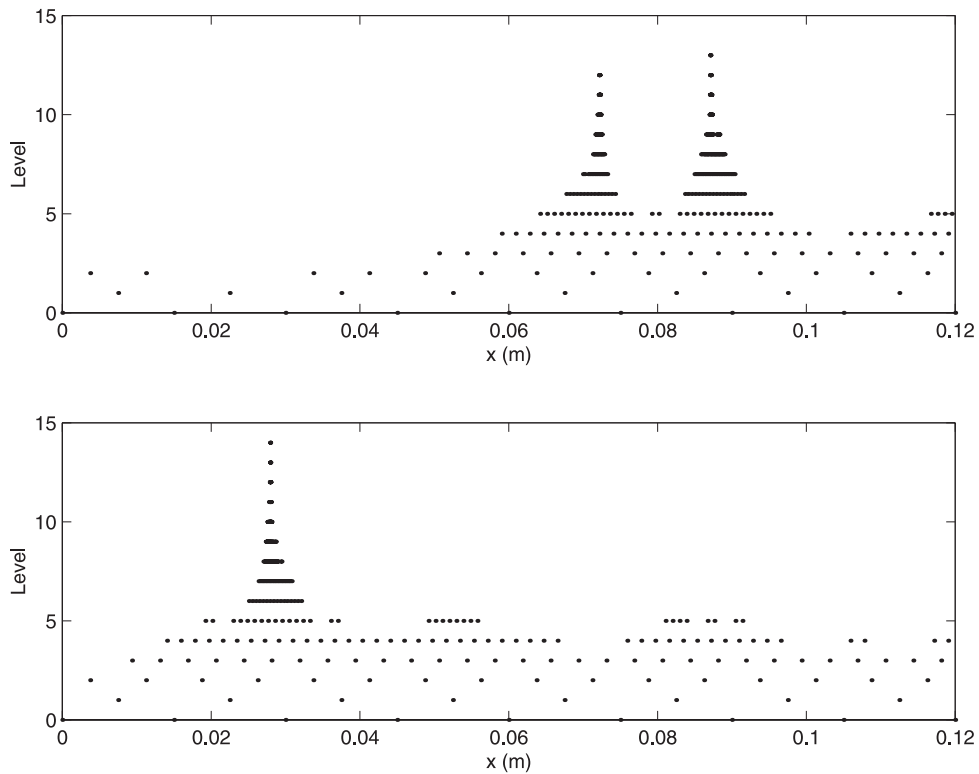


Figure 6. Spatial distribution of collocation points and levels at $t = 180 \mu\text{s}$ (two-shock structure) and $t = 230 \mu\text{s}$ (single-shock structure) demonstrating grid adaption.

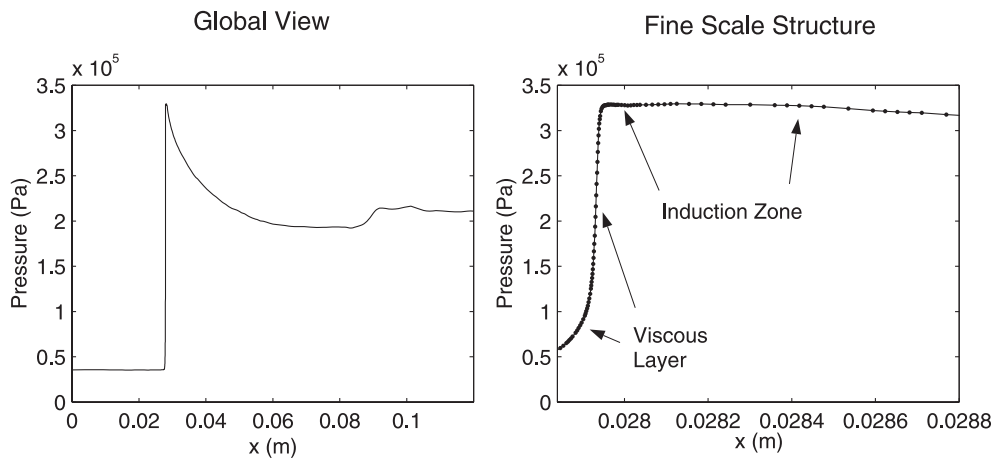


Figure 7. Predictions of pressure versus distance at $t = 230 \mu\text{s}$ on coarse and fine length scales demonstrating the spatial resolution of viscous and induction zone structures.

standard models of Maas and Warnatz [25] and Maas and Pope [3]. Such small time scales give rise to small reaction-induced spatial scales which violate the continuum assumption. It is essentially for this reason that we are not adapting our spatial grid to capture the subsequent

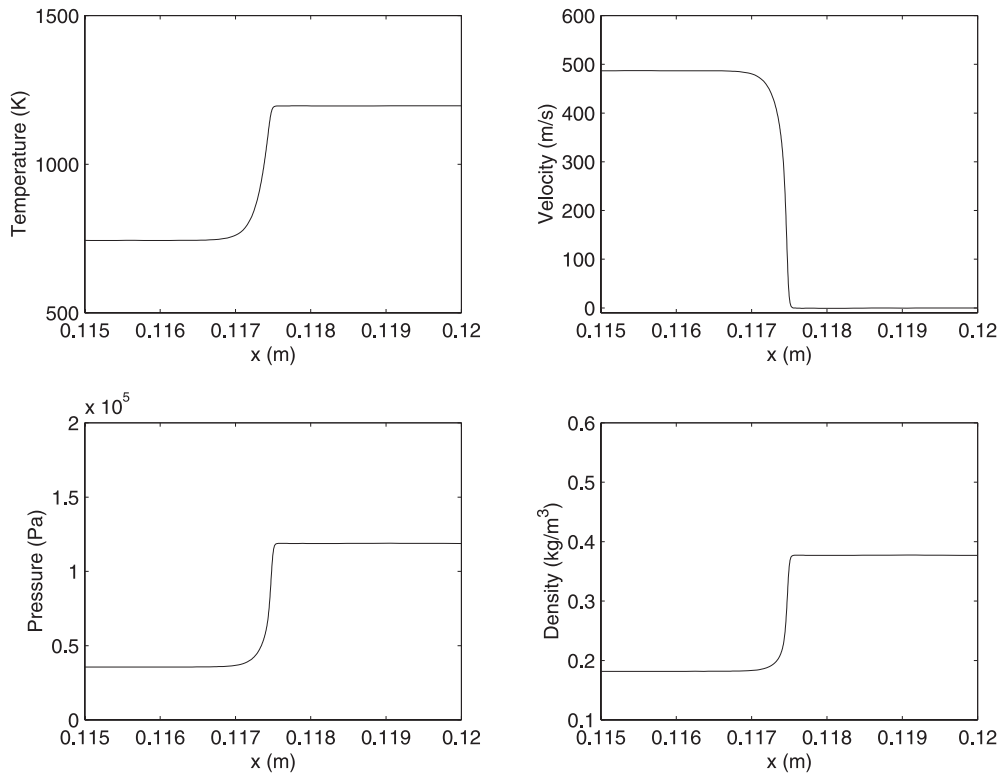


Figure 8. Predictions of temperature, velocity, pressure and density versus distance before commencement of significant reaction but after shock reflection using a reactive Navier–Stokes model, $t = 177 \mu\text{s}$.

extremely fine length scales associated with individual species mass fraction variation. This issue is pervasive in most calculations involving detailed chemical kinetics, but it is not often addressed since standard spatial discretization algorithms are unable to resolve this range of scales.

As discussed by Menikoff [21], inviscid codes introduce pseudo-entropy layers near regions of wave–wave and wave–boundary interactions. These often appear as $O(1)$ anomalies in temperature and density near the wall in shock tube predictions. Figure 8 shows the results of our viscous calculation in a spatial zone near the wall just after shock reflection. On this scale, there is no apparent entropy layer near the wall.

A finer scale examination of the dependent variables, shown in figure 9, reveals what is happening. It is evident from the temperature plot that there is a small entropy layer near the wall, here physically induced. The physical diffusion mechanisms rapidly smear the layer within a few microseconds. It may be possible that the correct capturing of a temperature-sensitive ignition event near a wall could be critically dependent on having the correct physics in the model. For the viscous calculation, a temperature rise of roughly 5 K is predicted. Performing a similar calculation with an inviscid Godunov-based model with first-order upwind spatial discretization near regions of steep gradients using 400 evenly spaced grid points induces a temperature rise of nearly 20 K, which persists. It might be expected that numerical diffusion would dissipate this temperature spike. However, as detailed by LeVeque [33], the leading-order numerical diffusion coefficient for such methods is proportional to the local fluid particle

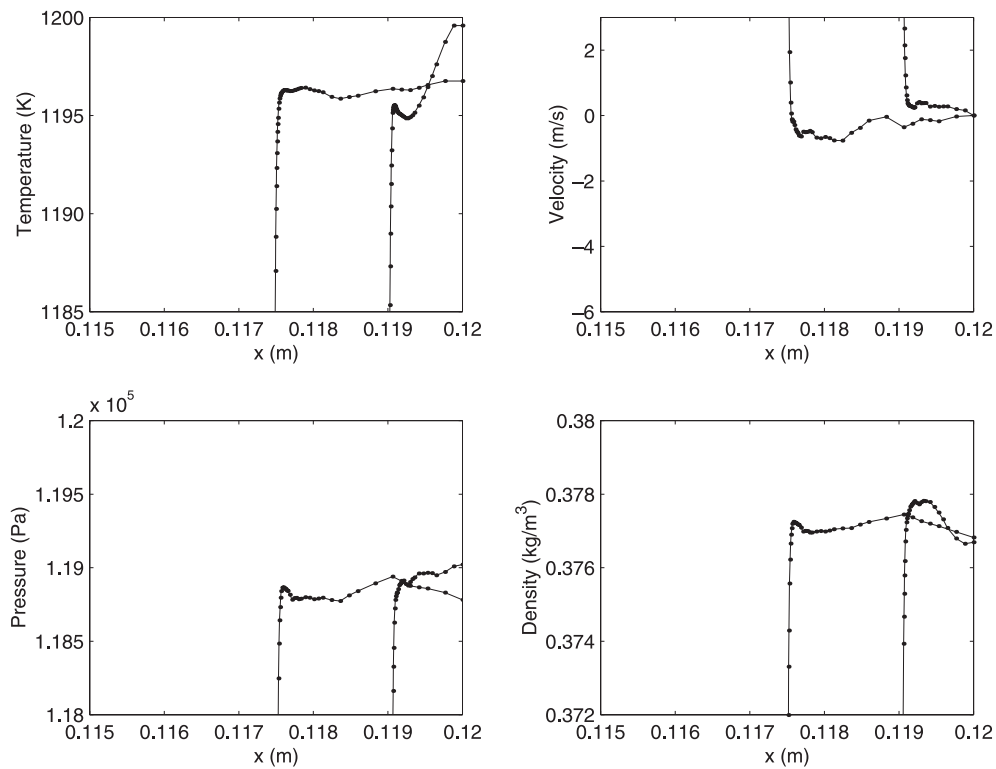


Figure 9. Close-up view of predictions of temperature, velocity, pressure and density versus distance before commencement of significant reaction but just after shock reflection ($t = 174 \mu\text{s}$) and slightly later ($t = 177 \mu\text{s}$).

velocity. As the fluid particle velocity at the wall and in the region downstream of the reflected shock is zero, the effects of numerical diffusion here are, at most, confined to higher order. This temperature rise, similar to that obtained by Fedkiw *et al* [16, 34], has been obtained by effectively imposing an adiabatic boundary condition through extrapolation. We note that this type of condition is inconsistent with the inviscid governing equations.

In concluding, we point out that decreasing the viscosity by an order of magnitude to the more appropriate value does not change the results, as the viscous and induction length scales (which are the smallest and next to smallest length scales, respectively) are sufficiently segregated. A decrease of the viscosity would simply further segregate these scales. Because of the segregation, there is little interaction between these scales. Thus reducing viscosity will only reduce the shock thickness.

In addition, the value of viscosity, be it physical or numerical, has a substantial effect on the entropy layer resulting from shock reflection, as discussed above. In order to properly capture this entropy layer, one must have a numerical viscosity which is much smaller than the physical viscosity. This is the case in our calculations and is clearly not in inviscid calculations. In inviscid calculations, the dynamics of the entropy layers are dependent upon the particular discretization employed as well as the artificial flux boundary conditions used.

The issues relating to scale segregation and entropy layer have been verified by performing calculations using a somewhat smaller value of viscosity without any notable changes from the results reported here.

6. Conclusions

The ILDM technique offers an effective way to rationally reduce detailed kinetic models; here, an effectively one-step model was used. The advantage is that the reduced model is guaranteed to maintain fidelity to full kinetic models to within a time scale which is easily determined. The WAMR technique allows the attainment of dramatic spatial resolution for flows, such as viscous hydrogen-oxygen-argon detonations, with widely disparate spatial scales. Here, thin viscous shocks, entropy layers and induction zones were fully resolved along with phenomena which evolved on much larger laboratory scales. While there are many challenges remaining for both methods, including how to efficiently build the higher-dimensional ILDMs which will be necessary to resolve finer time scales, and extending the WAMR technique to complex multidimensional geometry, it appears clear that these methods can be used effectively to solve problems with disparate length and time scales which are endemic in scientific computing.

Acknowledgments

This study was supported by NSF under CTS-9705150 and AFOSR under F49620-98-1-0206. The authors acknowledge many useful discussions with Dr Christopher Bowman, postdoctoral research associate at the University of Notre Dame.

References

- [1] Westbrook C K and Dryer F L 1981 Simplified reaction mechanisms for the oxidation of hydrocarbon fuels in flames *Combust. Sci. Technol.* **27** 31-43
- [2] Khokhlov A M, Oran E S, Chtchelkanova A Y and Wheeler J C 1999 Interaction of a shock with a sinusoidally perturbed flame *Combust. Flame* **117** 99-116
- [3] Maas U and Pope S B 1992 Simplifying chemical kinetics: intrinsic low-dimensional manifolds in composition space *Combust. Flame* **88** 239-64
- [4] Goussis D A and Lam S H 1992 A study of homogeneous methanol oxidation kinetics using CSP *24th Int. Symp. on Combustion* (Pittsburgh, PA: The Combustion Institute) pp 113-20
- [5] Blasenbrey T, Schmidt D and Maas U 1998 Automatically simplified chemical kinetics and molecular transport and its applications in premixed and non-premixed laminar flame calculations *27th Int. Symp. on Combustion* (Pittsburgh, PA: The Combustion Institute) pp 505-11
- [6] Eggels R L G M, Louis J J J, Kok J B W and DeGoey L P H 1997 Comparison of conventional and low-dimensional manifold methods to reduce reaction mechanisms *Combust. Sci. Technol.* **123** 347-62
- [7] Hamiroune D, Bishnu P, Metghalchi M and Keck J C 1998 Rate-controlled constrained-equilibrium method using constraint potentials *Combust. Theory Modelling* **2** 81-94
- [8] Lam S H 1993 Using CSP to understand complex chemical kinetics *Combust. Sci. Technol.* **89** 375-404
- [9] Schmidt D, Segatz J, Riedel U, Warnatz J and Maas U 1996 Simulation of laminar methane-air flames using automatically simplified chemical kinetics *Combust. Sci. Technol.* **113-4** 3-16
- [10] Norris A T 1998 Automated simplification of full chemical mechanisms: implementation *National Combustion Code AIAA Paper* 98-3987
- [11] Yang B and Pope S B 1998 An investigation of the accuracy of manifold methods and splitting schemes in the computational implementation of combustion chemistry *Combust. Flame* **112** 16-32
- [12] Yang B and Pope S B 1998 Treating chemistry in combustion with detailed mechanisms—*in situ* adaptive tabulation in principal directions—premixed combustion *Combust. Flame* **112** 85-112
- [13] Hadjinicolaou M and Goussis D A 1999 Asymptotic solution of stiff PDEs with the CSP method: the reaction diffusion equation *SIAM J. Sci. Comput.* **20** 781-810
- [14] Vasilyev O V and Paolucci S 1996 A dynamically adaptive multilevel wavelet collocation method *J. Comput. Phys.* **125** 498-512
- [15] Vasilyev O V and Paolucci S 1997 A fast adaptive wavelet collocation algorithm for multidimensional PDEs *J. Comput. Phys.* **138** 16-56
- [16] Fedkiw R P, Merriman B and Osher S 1997 High accuracy numerical methods for thermally perfect gas flows with chemistry *J. Comput. Phys.* **132** 175-90

- [17] Fedkiw R P, Merriman B and Osher S 2000 Simplified discretization of systems of hyperbolic conservation laws containing advection equations *J. Comput. Phys.* **157** 302–26
- [18] Oran E S, Young T R, Boris J P and Cohen A 1982 Weak and strong ignition. I. numerical simulations of shock tube experiments *Combust. Flame* **48** 135–48
- [19] Strang G 1968 On the construction and comparison of difference schemes *SIAM J. Numer. Anal.* **5** 506–17
- [20] Singh S, Powers J M and Paolucci S 1999 Detonation solutions from reactive Navier–Stokes equations *AIAA Paper* 99-0966
- [21] Menikoff R 1994 Errors when shock-waves interact due to numerical shock width *SIAM J. Sci. Comput.* **15** 1227–42
- [22] Merk H J 1959 The macroscopic equations for simultaneous heat and mass transfer in isotropic, continuous and closed systems *Appl. Sci. Res. A* **8** 73–99
- [23] Kee R J *et al* 1999 Transport: a software package for the evaluation of gas-phase, multicomponent transport properties *Chemkin Collection* Release 3.5 (San Diego, CA: Reaction Design, Inc)
- [24] Kee R J, Rupley F M and Miller J A 1990 The chemkin thermodynamic data base *Sandia National Laboratories Report* SAND87-8215B
- [25] Maas U and Warnatz J 1988 Ignition processes in hydrogen–oxygen mixtures *Combust. Flame* **74** 53–69
- [26] Williams F A 1985 *Combustion* (Menlo Park, CA: Benjamin-Cummings)
- [27] Warnatz J, Maas U and Dibble R W 1996 *Combustion* (Berlin: Springer)
- [28] Schott G L and Kinsey J L 1958 Kinetic studies of hydroxyl radicals in shock waves. II. induction times in the hydrogen–oxygen reaction *J. Chem. Phys.* **29** 1177–82
- [29] Hindmarsh A C 1983 ODEPACK, a systematized collection of ODE solvers *Scientific Computing* ed R S Stepleman *et al* (Amsterdam: North-Holland) pp 55–64
- [30] Reaction Design 1999 Chemkin-III, a software package for the analysis of gas-phase chemical and plasma kinetics *Reaction Design* CHE-035-1
- [31] Maas U 1998 Efficient calculation of intrinsic low-dimensional manifolds for the simplification of chemical kinetics *Computing Visualization Sci.* **1** 69–81
- [32] Golub G H and Van Loan C F 1996 *Matrix Computations* (Baltimore, MD: Johns Hopkins)
- [33] LeVeque R J 1992 *Numerical Methods for Conservation Laws* (Basel: Birkhäuser)
- [34] Fedkiw R P, Marquina A and Merriman 1999 An isobaric fix for the overheating problem in multimaterial compressible flows *J. Comput. Phys.* **148** 545–78